Moment Tensor Analysis

Masayasu Ohtsu

Abstract In order to determine kinematics of AE source, treatment of the moment tensor analysis is essential, because nucleation of cracks can be represented by the moment tensor. To this end, the SiGMA (Simplified Green's functions for Moment tensor Analysis) code is developed. Thus, crack kinematics on locations, types and orientations are determined three-dimensionally. Basic treatment and theoretical background are discussed, including the two-dimensional case. Theoretical backgrounds, relative sensor calibration for the analysis, eigen-value analysis of the tensor, visualization are comprehensively stated.

Keywords SiGMA code · Eigen-value analysis · Unified decomposition · Crack orientation · Visualization of AE sources

1 Introduction

In seismology, linear inversion techniques were proposed to determine the moment tensor component in both time and frequency domains (Stump and Johnson 1977; Kanamori and Given 1981). Although all the components of the moment tensor must be determined, the moment tensor inversion with constraints has been normally applied to obtaining stable solutions in seismology (Dziewonski and Woodhouse 1981). This is partly because a fault motion of an earthquake is primarily associated with shear-slip motion, corresponding to only off-diagonal components in the moment tensor. One application of the moment tensor inversion with constraints is found in rock mechanics (Dai et al. 2000).

In contrast, both tensile motion of diagonal components and shear motion of off-diagonal are definitely present in crack motions as an AE source. Consequently, general treatment on the moment tensor components of diagonal and off-diagonal components is discussed. Elsewhere, another procedure named the relative moment tensor inversion is proposed (Dahm 1996).

M. Ohtsu (✉)
Graduate School of Engineering, Kyoto University, Kyoto 615-8540, Japan
e-mail: ohtsu.masayasu.4v@kyoto-u.ac.jp

C. U. Grosse et al. (eds.), *Acoustic Emission Testing*, Springer Tracts in Civil Engineering, https://doi.org/10.1007/978-3-030-67936-1_8

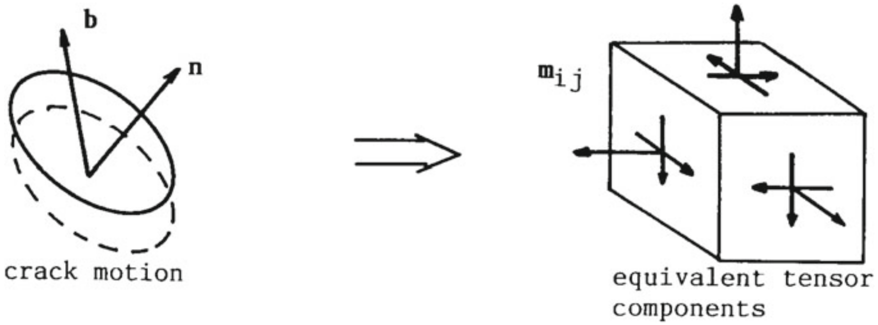

Fig. 1 Crack motion and equivalent tensor components

2 Theoretical Background

As discussed in chap. "Source Mechanisms", AE wave due to cracking is theoretically represented by the moment tensor M_{pq} as,

$$u_k(\mathrm{x}, t) = G_{ip,q}(\mathrm{x}, \mathrm{y}, t)M_{pq} * S(t) \tag{1}$$

The components of the moment tensor consist of crack motion (dislocation vector), the normal vector to the crack surface and crack the volume. Thus, crack motion is kinematically modeled by the components of the moment tensor as illustrated in Fig. 1.

To inversely solve Eq. 1 and to determine all the components of the moment tensor, the spatial derivatives of Green's functions are inevitably required. Accordingly, numerical solutions are obtained by the Finite Difference Method (FDM) (Enoki et al. 1986) and by the Finite Element Method (FEM) (Hamstad et al. 1999). These solutions, however, need a vector processor for computation and are not readily applicable to processing a large amount of AE waves. Consequently, based on the far-filed term of P wave, a simplified procedure was developed (Ohtsu et al. 1998), which is suitable for a PC-based processor and robust in computation. The procedure is now implemented as a SiGMA (Simplified Green's functions for Moment tensor Analysis) code. A source code is currently available in the State-of-the Art report of the RILEM Technical Committee 239-MCM (Ohtsu 2016).

3 Far-Field Approximation

Taking into account only P wave motion of the far field (1/R term) of Green's function in an infinite space, the displacement $U_i(\mathbf{x},t)$ of P wave motion is obtained from Eq. 1.

$$U_i(\mathrm{x},t) = \frac{1}{4\pi\rho v_p^3}\frac{r_i}{R} r_p r_q M_{pq}\frac{dS(t)}{dt} \tag{2}$$

Here ρ is the density of the material and v_p is the velocity of P wave. R is the distance between the source **y** and the observation point **x**, of which direction cosine is $\boldsymbol{r} = (r_1, r_2, r_3)$. In the case that we are interested in motions of AE waves at the observation point, the first approximation could be an elastic wave in a half space.

In the case that Eq. 2 is applied to the moment tensor analysis, the discrepancy between the half-space solution and the infinite-space solution should be examined. Accordingly, Lamb's solutions for buried pulse are compared with Green's functions in an infinite space.

As stated in chap. "Source Mechanisms", a code for computing Lamb's solution due to buried pulse was already published (Ohtsu and Ono 1984). An infinite-space solution is available in the literature (Aki and Richards 1980). Thus, a solution $\mathrm{UN_{ij}}$ in an infinite space due to a step-function force H(t) is obtained as,

$$\begin{aligned}
&\mathrm{UN_{ij}}(\mathbf{x},\mathbf{y},\mathrm{t}) = (3r_i r_j - \delta_{ij})/(4\pi\mu R)\\
&\left[\left\{(v_s t/R)^2 - \left(v_s/v_p\right)^2\right\} H(t-R/v_p)/2 - \{(\mathbf{v_s t/R})^2 - 1\}\mathrm{H}(t-R/v_s)/2\right]\\
&+ r_i r_j/(4\pi\mu R)\left\{\left(v_s/v_p\right)^2 \mathrm{H}(t-R/v_p) - \mathrm{H}(t-R/v_s)\right\}\\
&+ \delta_{ij}\mathrm{H}(t-R/v_s)/(\pi^2\mu R)
\end{aligned} \tag{3}$$

Taking only the far-field term out of Eq. 3,

$$\begin{aligned}
\mathrm{UF_{ij}}(\mathbf{x},\mathbf{y},t) = {} & r_i r_j/(4\pi\mu R)\left\{\left(v_s/v_p\right)^2 \mathrm{H}(t-R/v_p) - \mathrm{H}(t-R/v_s)\right\}\\
& + \delta_{\mathrm{ij}}\mathrm{H}(t-R/v_s)(\pi^2\mu R)
\end{aligned} \tag{4}$$

Here is the Lame constant and equivalent to shear modulus. v_s is the velocity of S wave.

In the x_1–x_2–x_3 coordinate system in Fig. 2, it assumed that step-function force f is applied in the x_3-direction at the depth 6 cm, and elastic waves in the x_3-direction are detected at three locations A, B, and C on the stress-free surface. The velocity of P wave is 4000 m/s and Poisson's ratio μ is 0.2. In order to investigate the discrepancy between the far-field approximation and the solutions in a half space, Lamb's solution G_{33}, infinite-space solution UN_{33}, and the far-field solution UF_{33} are computed.

Computed Green's functions at location A near an epi-center are shown in Fig. 3. Lamb's solution due to a step-function force shows clear arrivals of P wave and S wave again as denoted in Fig. 7.2a. The amplitude of the infinite-space solution is a half of that of Lamb's solution, while the far-field approximation is rather different from Lamb's solution, only show the dominant amplitude of P wave.

In the case that elastic waves are observed at a stress-free surface in a half space, reflected waves are generated and also detected as well as incident waves. In the case that incident S wave is reflected as P wave, a relationship between reflected angle θ

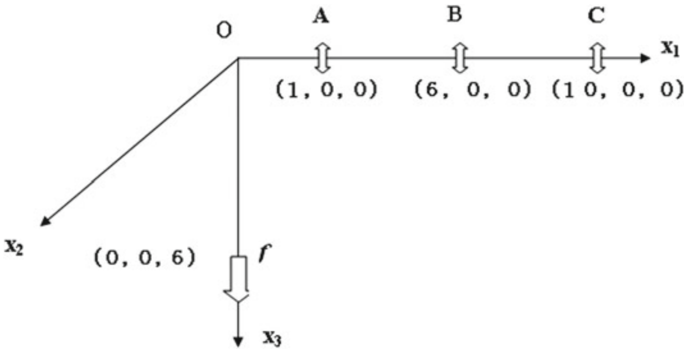

Fig. 2 Wave motions at locations A, B, and C on the stress-free surface due to a buried force ***f***

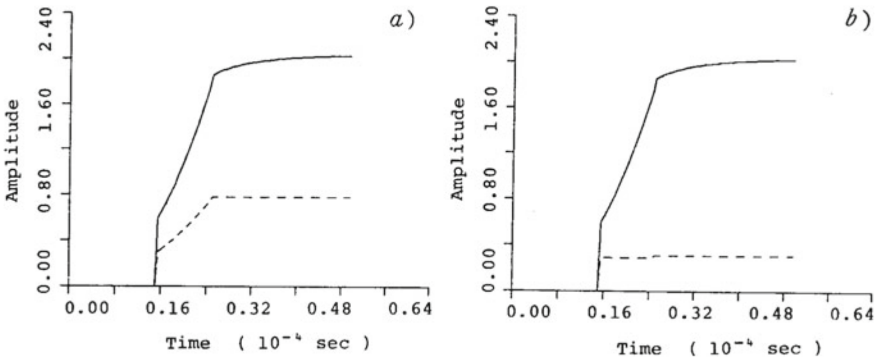

Fig. 3 Displacement motions detected at location A in a half space (solid curves in a) and b)), compared with solutions in an infinite space (broken curve in a)) and of the far-filed (broken curve in b))

of P wave and incident angle θ' is derived from Snell's law as,

$$\frac{\sin\theta}{v_p} = \frac{\sin\theta'}{v_s} \tag{5}$$

In the critical case of incident S wave, reflected P wave propagates along the surface (= /2), which is called SP wave and arrives at the observation point after P-wave arrival right before S-wave arrival as shown in Fig. 7.2(b). The critical angle θ'= θ*c* is obtained from $\sin^{-1}$ (v_s/v_p).

Green's functions at locations B and C are given in Figs. 4, and 5. In these cases, the incident angles are over the critical angle (θ*c* = 37.76°). Consequently, SP wave is observed at both locations. As a result, the difference from the infinite-space solution and the far-field solution is emphasized after P wave arrival.

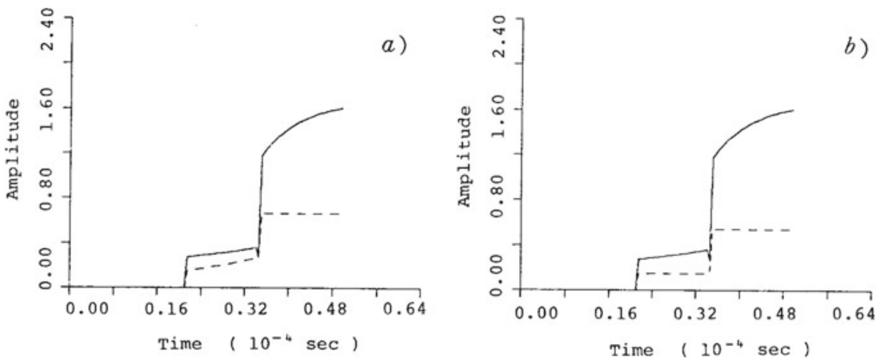

Fig. 4 Displacement motions detected at location B in a half space (solid curves in a) and b)), compared with solutions in an infinite space (broken curve in a)) and of the far-filed (broken curve in b))

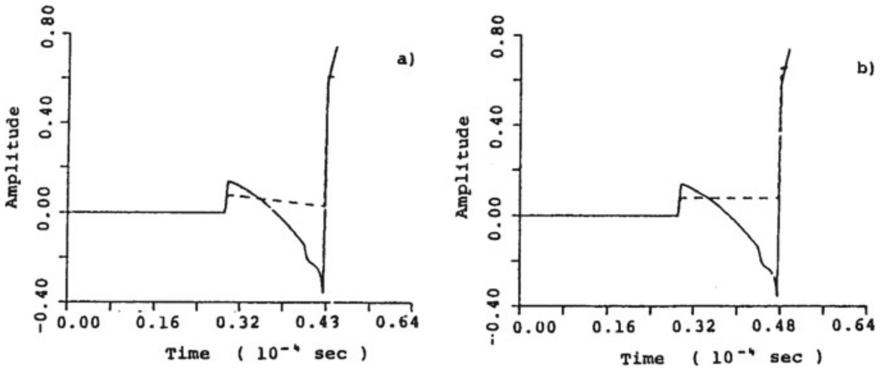

Fig. 5 Displacement motions detected at location C in a half space (solid curves in a) and b)), compared with solutions in an infinite space (broken curve in a)) and of the far-filed (broken curve in b))

In all the cases, it is concluded that the amplitude of the first motion (P wave) in a half space is almost as twice as the amplitudes of both the infinite-space solution and the far-filed solution. The ratio of the amplitude in a half space to that of the infinite space is equivalent to the reflection coefficient $Re(\mathbf{t}, \mathbf{r})$,

$$R_e(\mathrm{t}, \mathrm{r}) = \frac{2k^2a(k^2 - 2[1 - a^2])}{(k^2 - 2[1 - a^2])^2 + 4a[1 - a^2]\sqrt{k^2 - 1 + a^2}} \tag{6}$$

Here $\mathbf{t}$ is the orientation vector of sensor sensitivity and $k = v_p/v_s$ and a is the scalar product of vector $\mathbf{r}$ and vector $\mathbf{t}$. In the case that P wave is incident vertically to the surface ($a = 1$), $Re(\mathbf{t}, \mathbf{r})$ becomes equal to 2.

Consequently, it is found that the first motions of AE waves detected at the observation point can be approximated with the reasonable accuracy as the product of the far-field solution and the reflection coefficient.

4 Sensor Calibration

Considering the effect of reflection at the surface, the amplitude of the first motion $Ao(\mathbf{x},t)$ in the far-field due to an applied force $\boldsymbol{f}(t)$ is derived from Eq. 4 and represented as,

$$A_o = Cs\text{Re}(\text{t, r})\frac{f(t)}{R} \tag{7}$$

where *Cs* is the magnitude of the sensor response including material constants. In only the case that the sensors are absolutely calibrated, the coefficients *Cs* are known. In a general case, relative coefficients are readily obtained by a pencil-lead break test.

After the sensors are attached onto a specimen, a test is conducted as illustrated in Fig. 6. AE waves are recorded due to a pencil-lead break and then relative coefficients Cs are obtained from,

$$Cs = AoR/\text{Re}(\text{t, r}) \tag{8}$$

Thus, the relative calibration coefficient *Cs* of equivalent sensitivity is obtained for each sensor. In a few cases, absolutely calibrated sensors are available. In this

Fig. 6 Experiment for relative sensor calibration

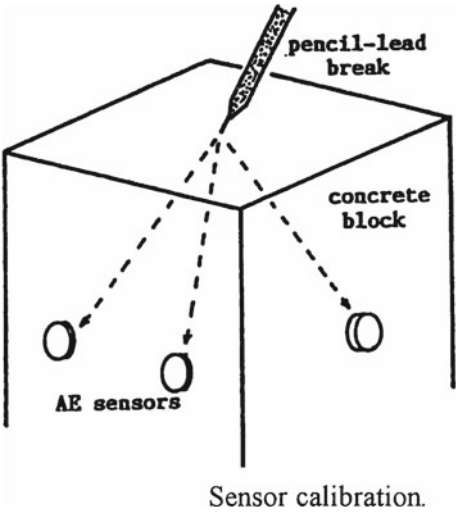

respect, the moment tensor analysis to determine the relative tensor components is preferable in practical applications.

5 SiGMA Procedure

Based on Eqs. 2 and 7, the amplitude of the first motion is simply represented as,

$$A(\mathrm{x}) = Cs\frac{\mathrm{Re(t, r)}}{R} r_p r_q M_{pq} \tag{9}$$

This leads to a series of algebraic equations on unknown moment-tensor components M_{pq}. The procedure to solve Eq. 9 is named SiGMA (Simplified Green's function for Moment tensor Analysis) (Ohtsu 1991, 2000). The algebraic equations to be solved are shown as,

$$A(\mathrm{x}) = Cs\frac{\mathrm{Re(t, r)}}{R}\begin{pmatrix} r_1 & r_2 & r_3 \end{pmatrix}\begin{pmatrix} m_{11} & m_{12} & m_{13} \\ m_{12} & m_{22} & m_{23} \\ m_{13} & m_{23} & m_{33} \end{pmatrix}\begin{pmatrix} r_1 \\ r_2 \\ r_3 \end{pmatrix} \tag{10}$$

Since the moment tensor is a symmetric tensor of the 2nd rank, the number of independent components is six as $m_{11}, m_{12}, m_{13}, m_{22}, m_{23}$, and m_{33}. These components can be determined from the observation of the first motions at more than six sensor locations. To solve Eq. 10, the coefficient *Cs*, the reflection coefficient *Re*(**t**, **r**), the distance *R*, and its direction cosine vector ***r*** are necessary. The determination of *Cs* and *Re*(**t**, **r**) is discussed in the previous sections. Other values can be obtained from the source (flaw) location analysis. Thus, the location analysis is essential to perform the moment tensor analysis.

In the SiGMA analysis, two parameters of the arrival time (P1) and the amplitude of the first motion (P2) are visually determined from AE waveform as shown in Fig. 7. In this respect, a computer-aided procedure was developed for automated determination of the first P-wave arrival (Ouyang et al. 1992) and (Ohno and Ohtsu 2010).

In the location procedure, the crack location **y** is determined from the arrival time differences $\mathrm{t_i}$ between the observation $\mathbf{x_i}$ and $\mathbf{x_{i+1}}$, solving equations,

$$\mathrm{R_i} - \mathrm{R_{i+1}} = |\mathbf{x_i} - \mathbf{y}| - |\mathbf{x_{i+1}} - \mathbf{y}| = \mathrm{v_p t_i} \tag{11}$$

Then, the distance *R* and its direction vector ***r*** are determined. The amplitudes of the first motions P2 in Fig. 7 at more than 6 channels are substituted into Eq. 10, and thus the components of the moment tensor are determined from a series of algebraic equations. Since the SiGMA code requires only relative values of the moment tensor components, the relative calibration coefficient *Cs* of AE sensors

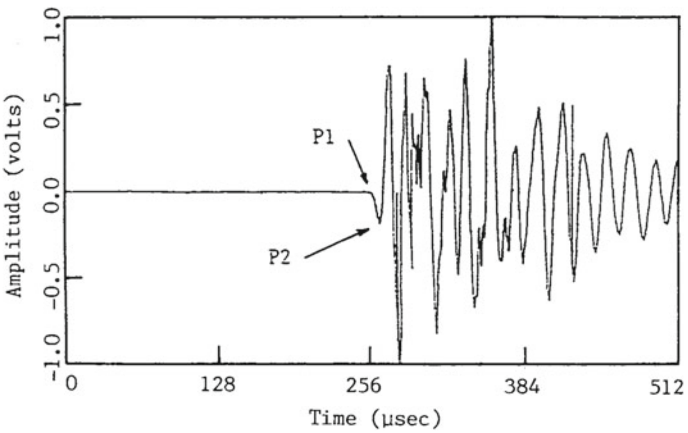

Fig. 7 Recorded AE waveform

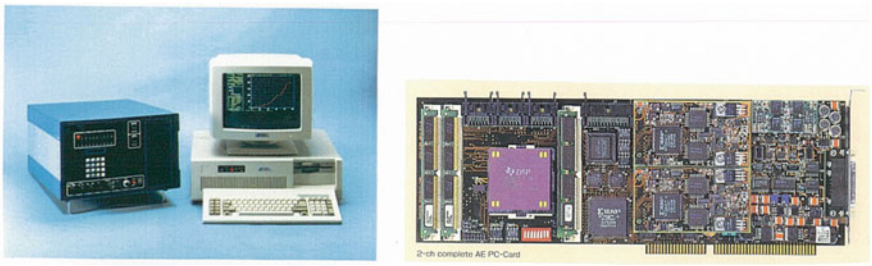

Fig. 8 AE device equipped with the SiGMA code

is sufficient enough. The code is already implemented in the AE device (Mistras- and Disp-TRA systems, PAC) as an example is shown in Fig. 8. A source code is also available in the State-of-the Art report of the RILEM Technical Committee 239-MCM (2016).

6 Unified Decomposition of Eigenvalue

In the SiGMA code, classification of a crack is performed by the eigenvalue analysis of the moment tensor (Ohtsu 1991). From Eq. 7.27, a moment tensor for pure shear motion is obtained as,

$$M_{pq} = \begin{pmatrix} 0 & 0 & \mu\Delta V \\ 0 & 0 & 0 \\ \mu\Delta V & 0 & 0 \end{pmatrix} \tag{12}$$

From the eigenvalue analysis, three eigenvalues are obtained as ΔV, 0, and $-\Delta V$. Setting the ratio of the maximum shear contribution as X, three eigenvalues for the shear crack are represented as X, 0, −X. In the case of a pure tensile crack, the moment tensor is represented from Eq. 7.26,

$$M_{pq} = \begin{pmatrix} \lambda\Delta V & 0 & 0 \\ 0 & \lambda\Delta V & 0 \\ 0 & 0 & (\lambda + 2\mu)\Delta V \end{pmatrix} \tag{13}$$

Because this is the case where the direction of crack motion is parallel to the coordinate axis, the matrix is already diagonalized, and diagonal components are identical to three eigenvalues: $\lambda\Delta V$, $\lambda\Delta V$, (+ 2)ΔV. In the case of the shear crack, the components of the tensor are deviatoric, as the sum of all components is equal to zero (non-volumetric). Accordingly, the components in Eq. 13 can be decomposed into the deviatoric (non-volumetric) components and the isotropic components as,

$$\begin{pmatrix} \lambda\Delta V \\ \lambda\Delta V \\ (\lambda + 2\mu)\Delta V \end{pmatrix} = \begin{pmatrix} -\frac{2\mu\Delta V}{3} \\ -\frac{2\mu\Delta V}{3} \\ \frac{4\mu\Delta V}{3} \end{pmatrix} + \begin{pmatrix} (\lambda + \frac{2\mu}{3})\Delta V \\ (\lambda + \frac{2\mu}{3})\Delta V \\ (\lambda + \frac{2\mu}{3})\Delta V \end{pmatrix} \tag{14}$$

Setting the ratio of the maximum deviatoric tensile component as Y and the isotropic tensile as Z, three eigenvalues are denoted as −Y/2 + Z, −Y/2 + Z and Y + Z. Then, it is assumed that the principal axes of the shear crack are identical to those of the tensile crack. As a result, the eigenvalues of the moment tensor for a general case are represented by the combination of the shear crack and the tensile crack. The following decomposition is obtained as the relative ratios X, Y and Z,

$$\begin{aligned} 1.0 &= \mathrm{X} + \mathrm{Y} + \mathrm{Z}, \\ \text{the intermediate eigenvalue/the maximum eigenvalue} &= 0 - \mathrm{Y}/2 + \mathrm{Z}, \\ \text{the minimum eigenvalue/the maximum eigenvalue} &= -\mathrm{X} - \mathrm{Y}/2 + \mathrm{Z}. \end{aligned} \tag{15}$$

These are schematically shown in Fig. 9. It should be pointed out that the ratio X becomes larger than 1.0 in the case that both the ratios Y and Z are negative (Suaris and van Mier 1995). The case happens, if the scalar product $l_k n_k$ is negative. Re-correcting the value of the scalar product, the three ratios are determined as well-posed.

Another decomposition of the moment tensor is proposed elsewhere (Shah and Labuz 1995), introducing the term of the volume change. As can be seen in Fig. 8, however, the ratio Z clearly represents the volume change. Addition of other terms is to be unnecessary.

The ratios X, Y, and Z are mathematically determined in an isotropic solid. Setting the angle, c, between crack vector $\boldsymbol{l}$ and normal vector to the crack surface $\boldsymbol{n}$, these are obtained as,

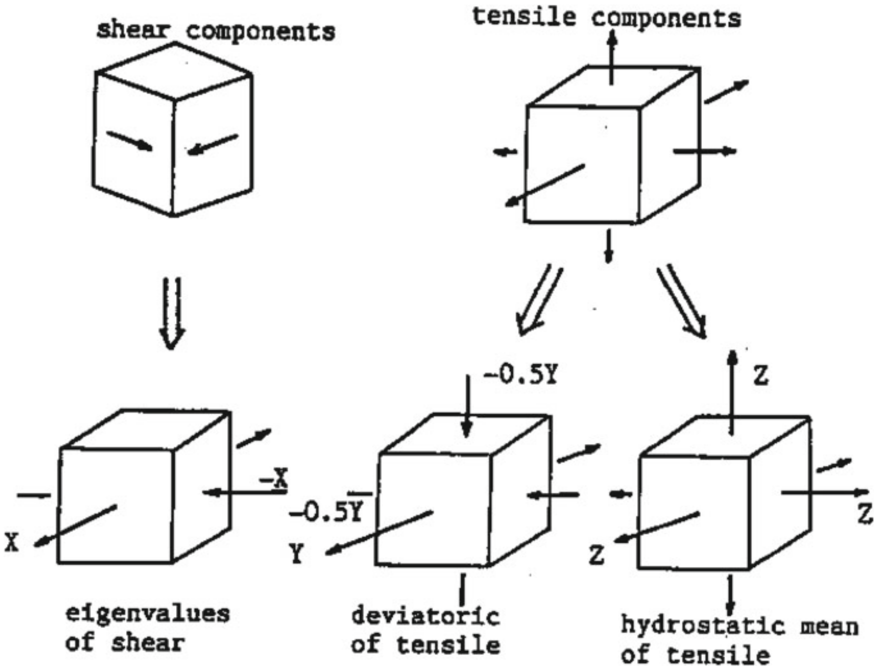

Fig. 9 Unified decomposition of eigenvalues of the moment tensor

$$
\begin{aligned}
\mathrm{X} &= [(1-2n)-(1-2n)\cos c]/[(1-2n)+\cos c],\\
\mathrm{Y} &= 4(1-2n)\cos c/[3(1-2n)+3\cos c],\\
\mathrm{Z} &= 2(1+n)\cos c/[3(1-2n)+3\cos c],
\end{aligned}
\tag{16}
$$

where $\cos c = l_k n_k$. The ratio X represents the contribution of shear motion. The raio Y is the contribution of deviatoric component of tensile motion, and the ratio Z is that of isotropic component. Hereinafter, the ratio X is called the shear ratio. Elsewhere, the classification of cracks was conducted on the basis of the angle c between two vectors $\boldsymbol{l}$ and $\boldsymbol{n}$ (Enoki et al. 1986). So, a relation between 1 - cos c and the shear ratio X is plotted in the case that Poisson's ratio = 0.2 in Fig. 8.10.

In a previous literature (Landis et al. 1992), cracks were classified as a tensile crack (mode I) in the case 0° < c<15°, which corresponds almost to a pure tensile crack as the shear ratio less than 5%. In contrast, shear cracks (mode II) were classified with the condition 75° < c<90°, in which the shear ratio X is just over 50%. Thus, the criterion on the crack classification based on the angle c seems to be not reasonable, because the relationship between the angle c and the shear ratio X is nonlinear. In the SiGMA code, AE sources of which the shear ratios are less than 40% are classified into tensile cracks. The sources of X > 60% are classified into shear cracks. In between 40 and 60%, cracks are referred to as mixed mode.

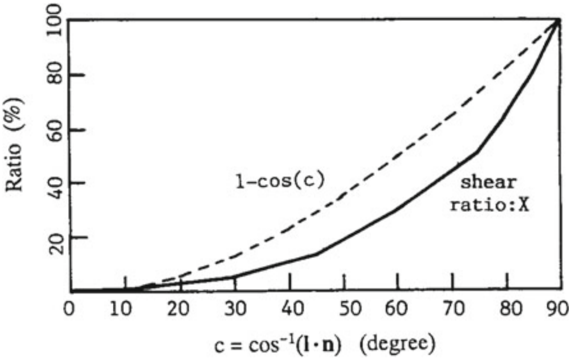

Fig. 10 Relation between shear ratios X and crack angles

7 Crack Orientation

From the eigenvalue analysis of the moment tensor, three eigenvectors ***e1***, ***e2***, ***e3*** are also obtained. These are presented by the two vectors ***l*** and ***n***,

$$\begin{aligned} e1 &= \mathbf{l} + \mathbf{n} \\ e2 &= \mathbf{l} \times \mathbf{n} \\ e3 &= \mathbf{l} - \mathbf{n}. \end{aligned} \tag{8.17}$$

Here x denotes the vector product, and the vectors ***l*** and ***n*** are interchangeable. In the case of the tensile crack, the vector ***l*** is parallel to the vector ***n***. Thus, the vector ***e1*** could give the direction of crack opening, while the sum of ***e1*** + ***e3*** and the subtraction ***e1*** − ***e3*** derive the two vectors ***l*** and ***n***.

In the first version of SiGMA (Ohtsu 1991), the orientations of tensile cracks are determined from the vector ***e1***, and those of shear cracks are presented by two vectors ***l*** and ***n***, which are usually perpendicular.

One result which was analyzed in a hydro-fracturing test is shown in Fig. 11. Eight AE events are analyzed and plotted in the elevation view. AE events are plotted at their locations from the location analysis. Then, cracks are classified based on the shear ratio. Tensile crack are indicated by arrow symbols, of which directions are determined from the direction ***e1***. Shear cracks are represented by cross symbols, of which two directions correspond to the two vectors ***l*** and ***n***. The event No. 14 was classified into the mixed-mode cracking, and both orientations of the tensile and the shear are indicated. Results are so successful that AE events are located along the dip plane presumed from the dip angle. Remarkably, the directions of crack opening of the tensile cracks are vertical to, and the orientations of the shear cracks seem parallel to the dip plane.

According to the result in Fig. 10, a crack of which angle is over 60° could be classified as the tensile crack, because the shear ratio is less than 40%. Consequently, In another version of SiGMA (Ohtsu 2000), two vectors are always obtained and

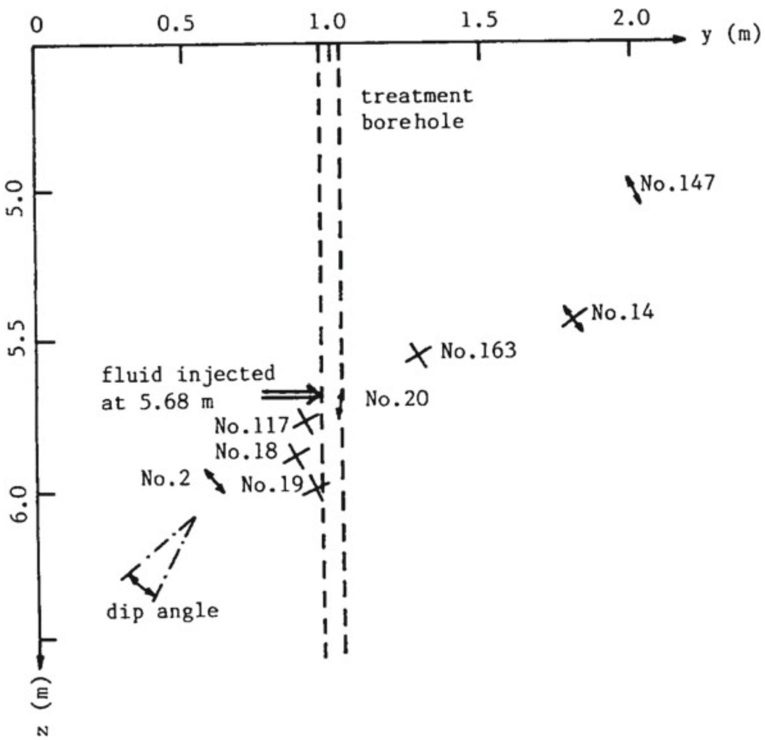

Fig. 11 Results of SiGMA analysis in a hydro-fracturing test

plotted. For the tensile crack, arrow symbol is employed. One result in a bending test of a reinforced concrete beam is given in Fig. 12 (Ohtsu 1995).

8 Two-Dimensional Treatment

A similar treatment can be applied to two-dimensional (2-D) problems. Deformations of the plate are classified into two motions. As illustrated in Fig. 13, one is in-plane motion where a crack surface is generated as the normal vector to the crack plane is vertical to the x_3-axis and AE waves are detected at the edge of the plate. The other is out-of-plane motion where the crack surface is created parallel to the x_1-x_2 plane. In the case of in-plane motions, the x_3-components in Fig. 8.14 of both the vector ***l*** and ***n*** are equal to zero. Then, the moment tensor in an isotropic solid becomes,

$$M_{pq} = \begin{pmatrix} \lambda l_k n_k + 2\mu l_1 n_1 & \mu(l_1 n_2 + l_2 n_1) & 0 \\ \mu(l_1 n_2 + l_2 n_1) & \lambda l_k n_k + 2\mu l_2 n_2 & 0 \\ 0 & 0 & \lambda l_k n_k \end{pmatrix} \Delta V \tag{18}$$

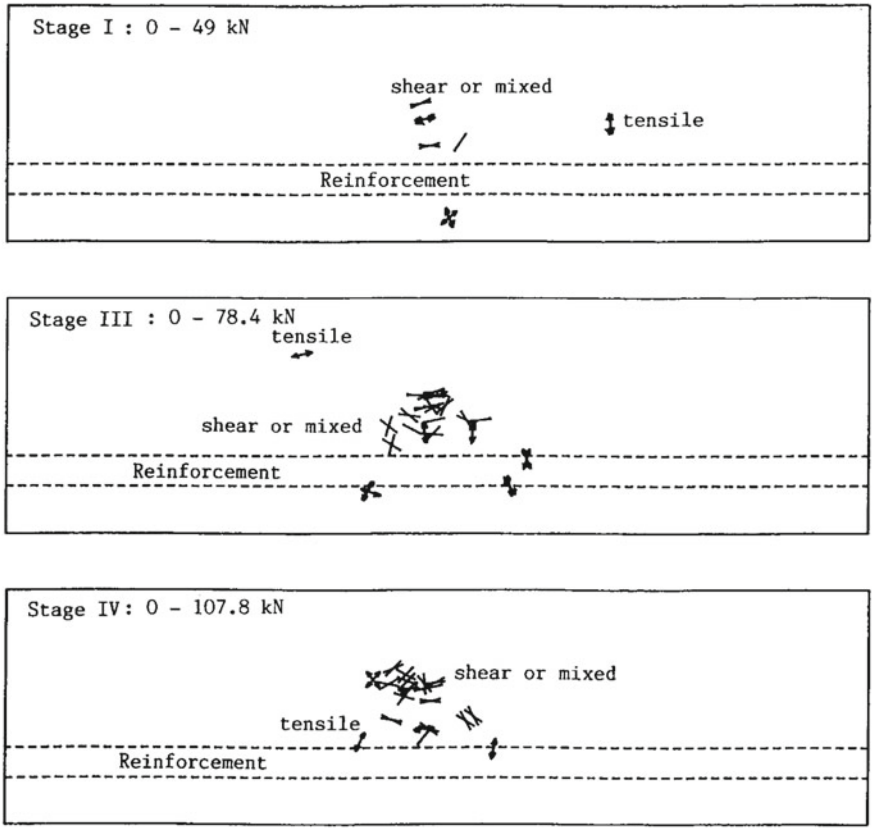

Fig. 12 Results of SiGMA analysis in a reinforced concrete beam under bending

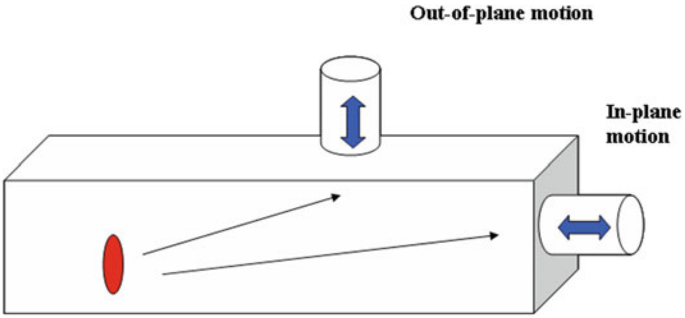

Fig. 13 AE detection in a plate specimen

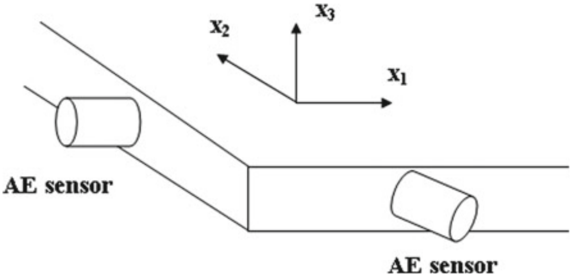

Fig. 14 AE detection (in-plane) at the edge of the plate

In the case that AE sensors are attached at the edge of the plate, the components of the tensor in Eq. 18 are readily defined except m_{33} component, because no motion in the x_3-direction is detected. The m_{33} component is actually determined from the following equation (Shigeishi and Ohtsu 1999),

$$m_{33} = ll_k n_k = l(m_{11} + m_{22})/(2l + 2m) = n(m_{11} + m_{22}). \tag{19}$$

In the case of in-plane observation in Fig. 14, the component of the moment tensor: m_{11}, m_{12}, m_{22} are easily determined, solving the following equation,

$$A(\mathrm{x}) = Cs\frac{R_e(\mathrm{t,r})}{R}\begin{pmatrix} r_1 & r_2 \end{pmatrix}\begin{pmatrix} m_{11} & m_{12} \\ m_{12} & m_{22} \end{pmatrix}\begin{pmatrix} r_1 \\ r_2 \end{pmatrix}$$

Since the m_{33} component is readily obtained from Eq. 19, the unified decomposition of the eigenvalues and the orientation analysis by the eigenvectors are to be performed in the same manner as those of the 3-D problems.

In the case of the out-of-plane observation, in contrast, only the case that a tensile crack is generated parallel to the x_1–x_2 plane in Fig. 14 can be treated. Even though the shear motion exists, theoretically no information can be recovered.

To locate AE sources, 5-channel system is at least necessary for three-dimensional (3-D) analysis. Since 6-channel system is the minimum requirement, 6-channel system is required for SiGMA. In contrast, 3-channel system is available for the 2-D analysis. One application is given in Fig. 15 (Shigeishi and Ohtsu 1999). Uniaxial stress is applied vertical to the plate specimen made of concrete, which contains a through-thickness slit. 4-channel system was employed for the measurement. Results show the case that slit angle to the loading axis is equal to 45°.

9 Estimation of Crack Volume

From the representation of the moment tensor, it is found that the trace components of the moment tensor is obtained as,

Fig. 15 Results of an in-plane problem

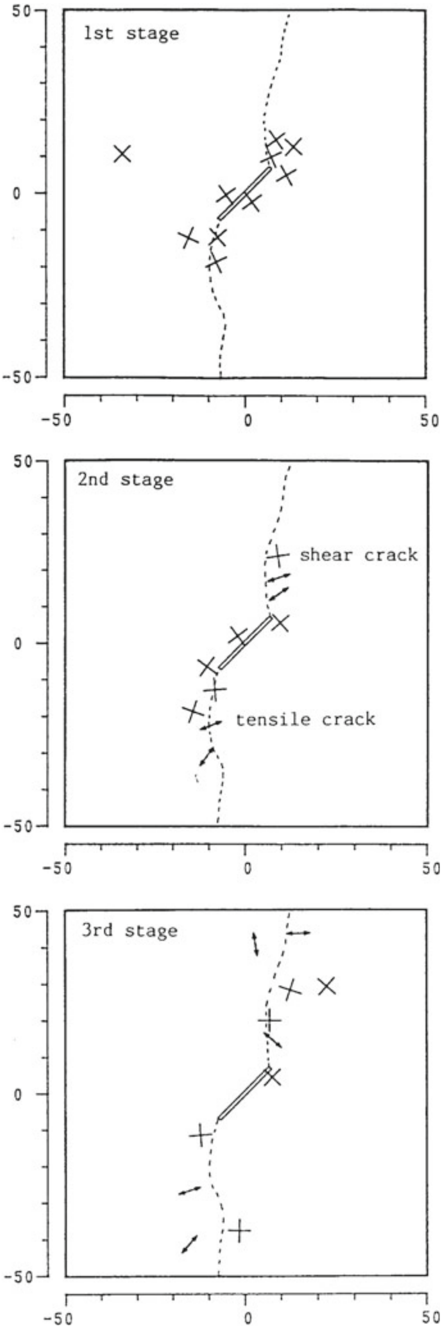

$$M_{kk} = (3l + 2m)l_k n_k DV. \tag{20}$$

One parameter in damage mechanics is defined (Kachanov 1980) as,

$$D = \int n_i \left(b_i n_j\right) n_j dS = DVl_k n_k = M_{kk}/(3l + 2m) \tag{21}$$

From Eqs. 20 and 21, the crack volume can be derived as,

$$DV = M_{kk}/[(3l + 2m)l_k n_k]. \tag{22}$$

where M_{kk} represents the trace components of the moment tensor. As mentioned, and are Lame constants.

Equation 22 implies that the process of damage evolution due to expansion of crack volumes is also estimated from the moment tensor analysis. One example is given in Fig. 16. From moment tensors determined in bending tests of concrete specimens with a notch (Ohtsu and Ohtsuka 1998), the damage evolution due to accumulation of

Fig. 16 Damage evolution analyzed from the moment tensor analysis

(a) type CC : concrete

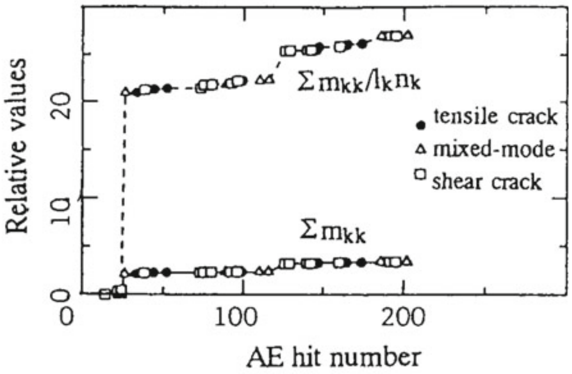

(b) type OC : mortar

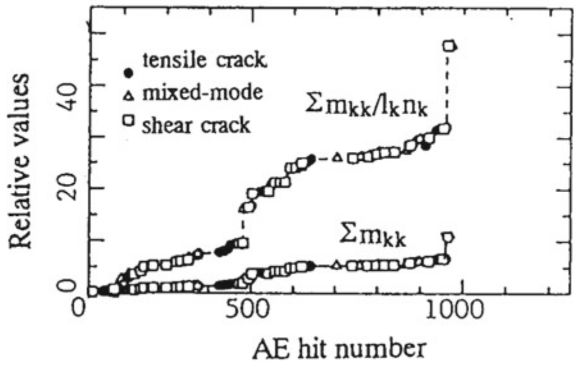

crack volumes is estimated. In the case of the center-notched specimen (type CC), the damage suddenly increases, while the damage evolution is gradual in the off-center notched specimen (type OC).

10 Error Estimation

Estimation of errors in the moment tensor analysis is fairly difficult (Landis et al. 1992). In the analysis of Fig. 11 (Ohtsu 1991), the conditioning numbers were estimated. As an attempt, error estimation was conducted, assuming the errors. It was found that the error estimation was such a complicated task that the errors were really dependent on spatial relations between located sources and observation points. In this regard, a post analysis was proposed (Ohtsu 2000), where AE waves to be detected at the observation points were synthesized from the source location and the moment tensor. For the simulation analysis of theoretical AE waves, the technique discussed in chap. "Source Mechanisms" is available.

By using the same size of a PMMA plate as given in Fig. 15, the leakage test was conducted (Ohno et al. 2006) 102 AE events with detectable first arrivals were analyzed by the two-dimensional SiGMA analysis. Results are classified by the shear ratio X (%) and listed in Table 1. It is clearly found that almost 60% events have the shear ratios over 60%. This implies that dominant source motions at the slit-like defect due to leakage are of in-plane shear-type. It was, however, realized that AE sources were distributed widely on the specimen, not concentrated around the slit. These might result from the fact that only large AE events were identified as the burst-type and readable for the analysis. In addition, determination of both the amplitude of the first motion and the arrival time was actually not an easy task. This implies that some errors are unwillingly contained in results of the SiGMA analysis.

Consequently, the post analysis was performed. AE waveforms at sensor locations were synthesized in an infinite space, taking into the source location and the moment tensor components. The reflection coefficient was taken into consideration to simulate the waveforms. The SiGMA procedure was applied to synthetic waveform set as the post analysis. Results are also given in Table 8.1. Because one event was located out of the specimen, results of 101 events are shown. In these results, location errors between the SiGMA analysis and the post analysis were within 1 mm. But, the shear ratio changed drastically as found in the table. Following the post analysis, events

Table 1 Results of SiGMA-2D analysis

Shear ratio (%)	0–40 (%) tensile	40–60 (%) mixed-mode	60–100 (%) shear
SiGMA analysis	20	20	62
Post analysis	12	10	79

Table 2 Reliable solution selected after the post analysis

Shear ratio (%)	0–40 (%) tensile	40–60 (%) mixed-mode	60–100 (%) shear
No. of events	10	3	33

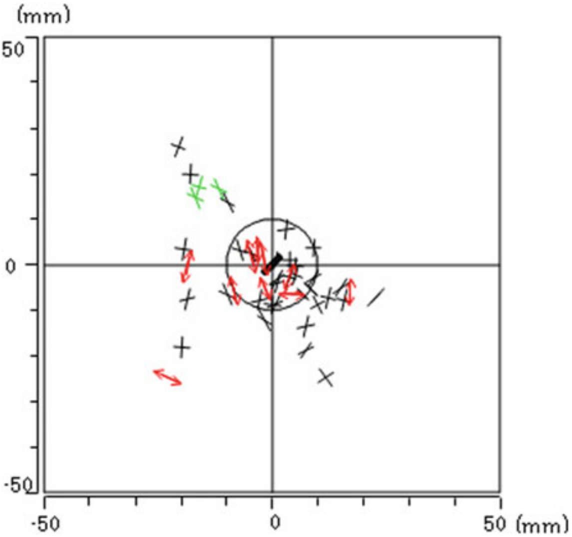

Fig. 17 Results of the post analysis

of the shear ratio less than 10% different from those of the SiGMA analysis were selected as reliable solutions. 46 events were selected and are listed in Table 8.2.

Kinematics of these 46 events are plotted in Fig. 8.17. Here, shear and mixed-mode cracks are indicated with cross symbol, and tensile cracks are denoted by arrow symbol. In the all cracks, directions of crack normal and crack motion are illustrated. It is found that AE sources of tensile types are mostly concentrated inside the pipe, where water pressure is applied. The opening directions of tensile cracks are almost vertical to the slit surface, suggesting that water flow due to leakage expands the slit.

11 Visualization of SiGMA Results

Visualization of the SiGMA results are to be made by employing softwares commercially available. By applying VRML (Virtual Reality Modeling Language), crack modes of tensile, mixed-mode and shear are given in Fig. 18. Here, an arrow vector indicate a crack motion vector, and a circular plate corresponds to a crack surface, which is perpendicular to a crack normal vector.

Experiments were conducted by using the same reinforcement concrete beams as shown in Fig. 12. As shown in Fig. 19a, at the first stage, a few tensile cracks (green) and mixed-mode cracks (red) are mostly observed near reinforcement at the

(a) tensile crack (b) shear crack (c) mixed-mode

Fig. 18 3-D display models for tensile, shear, and mixed-mode cracks

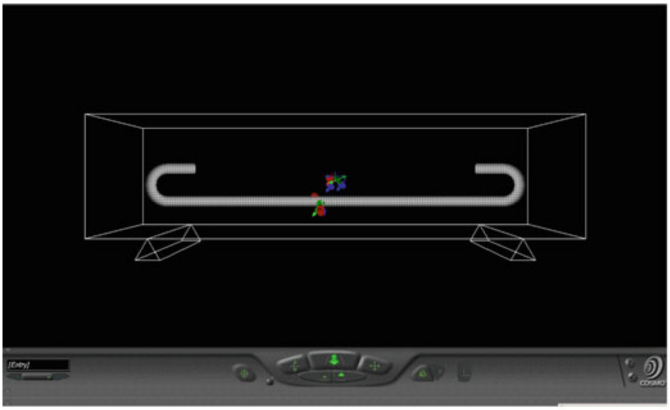

(a) 1^{st} stage

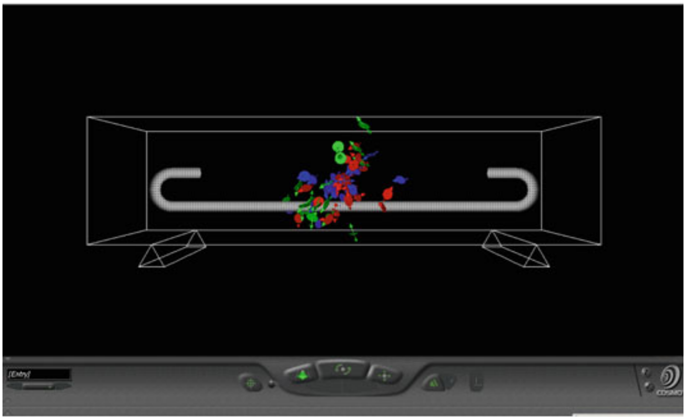

(b) Intermediate Stage

Fig. 19 Results of SiGMA analysis visualized by VRML

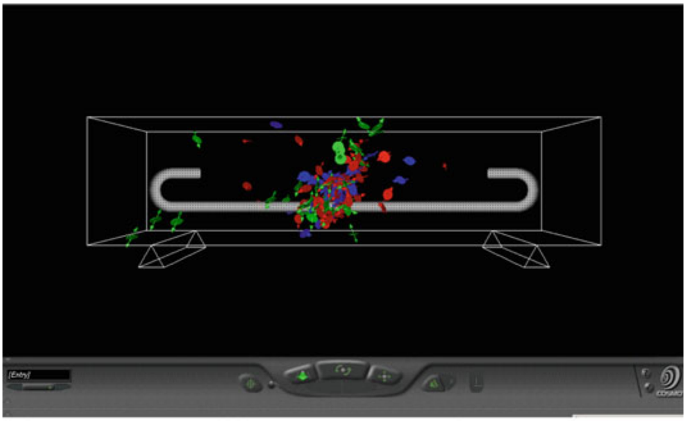

(c) Final stage

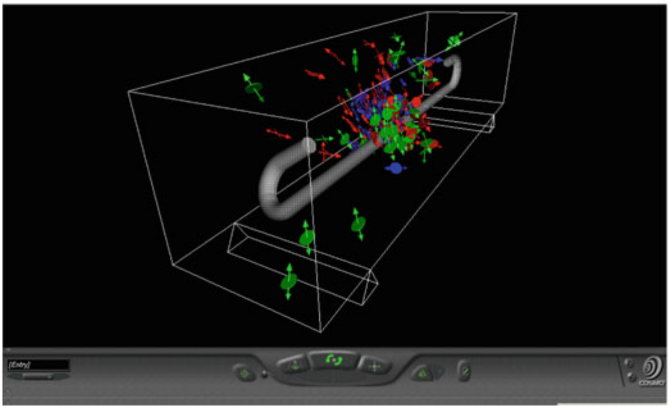

(d) Visualization from an inclined angle.

Fig. 19 (continued)

central region. Then, delamination between concrete and reinforcement occurred. Activity of cracking increased as the increase in mixed-mode cracks. Bending cracks were visually observed. The tips of cracks extended upward, penetrating into the compressive zone of the upper half. Thus, at the intermediate stage in Fig. 19b, AE cluster expands upward, increasing the number of shear cracks (blue). The cracks then stopped due to compression, and the beam reached final failure of diagonal-shear failure or concrete crashing at the upper half. Approaching the final stage in Fig. 19c, d, cluster of AE sources further expands and nucleation of cracks is really mixed up of tensile, mixed-mode, and shear cracks. Cracks distribute widely, probably corresponding to nucleation of diagonal shear cracks between the loading point and the support. Locations and orientations of the source can be visually identified.

Another example of the SiGMA results is visuallized in Fig. 20. In a reinforced concrete (RC) beam, diagonal-shear failure was generated in the shear span without

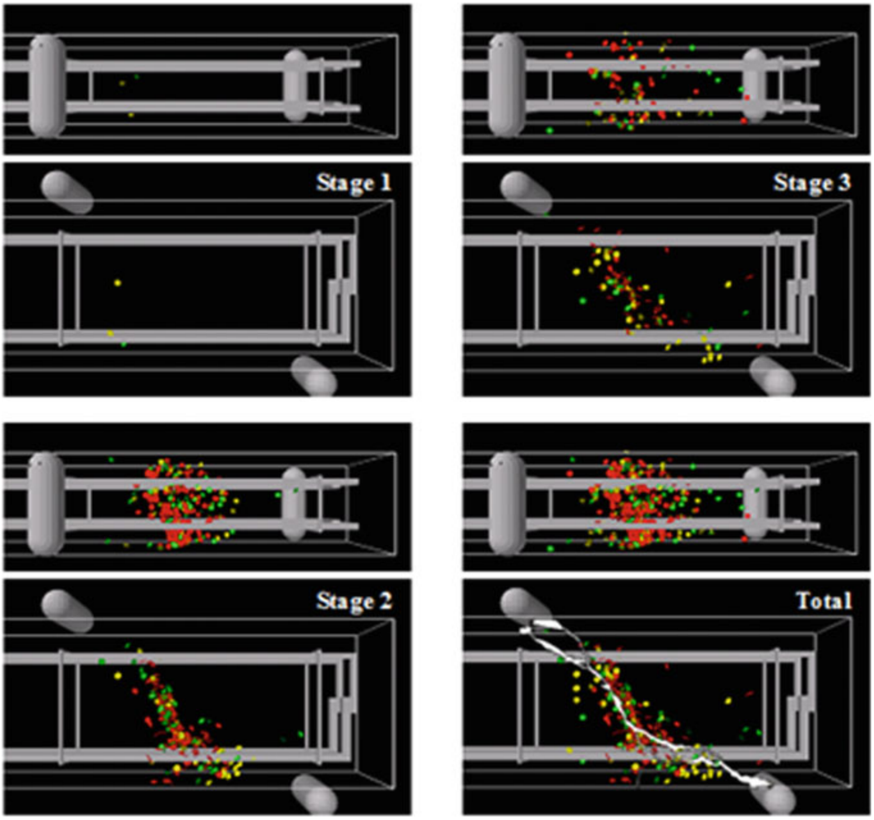

Fig. 20 Visualized results of the SiGMA analysis in diagonal-shear failure of RC beam

stirrup reinforcement (Ohno and Ohtsu 2010). AE measurement was conducted by using 8 sensors, which were arrayed in the one-side of shear spans. It is clearly observed that final AE cluster is in remarkable agreement with the failure surface of diagonal-shear.

12 Concluding Remarks

Nucleation of cracks can be kinematically analyzed by the moment analysis. Applying the SiGMA (Simplified Green's functions for Moment tensor Analysis) code, crack kinematics on locations, types and orientations are determined three-dimensionally. Basic treatment and theoretical background are discussed, including the two-dimensional case.

For the two-dimensional solution, in-plane motions of AE waves are treated. As a practical application, AE waves due to water leakage from a slit are detected and analyzed. The reliable solutions are selected by the post analysis. Because visualization of results is desirable, 3-D visualizations of the SiGMA results are illustrated and discussed.

References

Aki K, Richards PG (1980) Quantitative seismology: theory and methods, vol I. W. H. Freeman and Company, San Francisco

Dahm T (1996) Relative moment tensor inversion based on ray theory: theory and synthetic tests. Geophys J Int 124:245–257

Dai ST, Labuz JF, Carvalho F (2000) Softening response of rock observed in plane-strain compression. Trends in Rock Mechanics, Geo SP-102, ASCE, pp 152–163

Dziewonski AM, Woodhouse JH (1981) An experiment in systematic study of global seismicity: centroid-moment tensor solutions for 201 moderate and large earthquakes of 1981. J Geophys Res 88(B4):3247–3271

Enoki M, Kishi T, Kohara S (1986) Determination of micro-cracking moment tensor of quasi-cleavage facet by AE source characterization. Progress in Acoustic Emission III, JSNDI, pp 763–770

Hamstad MA, O'Gallagher A, Gary J (1999) Modeling of buried monopole and dipole source of acoustic emission with a finite element technique. J AE 17(3–4):97–110

Kachanov M (1980) Continuum model of medium with cracks. J Eng Mech ASCE 106(EM5):1039–1051

Kanamori H, Given JW (1981) Use of long-period surface waves for fast determination of earthquake source parameters. Phys Earth Planet Inter 27:8–31

Landis E, Ouyang C, Shah SP (1992) Automated determination of first P-wave arrival on acoustic emission source location. J AE 10(1/2):s97–s103

Ohno K, Suzuki T, Shimozono S, Ohtsu M (2006) Moment tensors of in-plane AE waves analyzed by SiGMA-2D. Progress in AE XIII, JSNDI, pp 239–246

Ohno K, Ohtsu M (2010) Crack classification in concrete based on AE. Constr Build Mater 24(1):2339–2346

Ohtsu M, Ono K (1984) A generalized theory of acoustic emission and Green's functions in a half space. J AE 3(1):124–133

Ohtsu M (1991) Simplified moment tensor analysis and unified decomposition of AE source: application to in situ hydrofracturing test. J Geophys Res 96(B4):6211–6221

Ohtsu M (1995) Acoustic emission theory for moment tensor analysis. Res Nondestr Eval 6:169–184

Ohtsu M, Okamoto T, Yuyama S (1998) Moment tensor analysis of acoustic emission for cracking mechanisms in concrete. ACI Struct J 95(2):87–95

Ohtsu M, Ohtsuka M (1998) Damage evolution by AE in the fracture process zone of concrete. J Mater Conc Struct Pavement, JSCE, 599/V-40:177–184

Ohtsu M (2000) Moment tensor analysis of AE and SiGMA code. Acoustic Emission-Beyond the Millennium. Elsevier, pp 19–34

Ohtsu M (ed) (2016), Innovative AE and NDT techniques for on-site measurement of concrete and masonry structures. Springer

Ouyang C, Landis E, Shah SP (1992) Damage assessment in concrete using acoustic emission. Nondestructive testing of concrete elements and structures. ASCE, pp 13–24

Shah KR, Labuz JF (1995) Damage mechanisms in stressed rock from acoustic emission. J Geophys Res 100(B8):15527–15539

Shigeishi M, Ohtsu M (1999) Identification of AE sources by using SiGMA-2D moment tensor analysis. Acoustic Emission: Standard Technol 1353:175–188

Stump BW, Johnson LR (1977) The determination of source properties by the linear inversion of sesimograms. Bull Seismo Soc Am 67(6):1489–1502

Suaris W, van Mier JGM (1995) Acoustic emission source characterization in concrete under biaxial loading. Mater Struct 28:444–449